Laboratory bistatic synthetic aperture radar coherent change detection investigation

Alexander Hagelberg,[1,✉] Daniel Andre,[1] and Mark Finnis[2]
[1]*Centre for Electronic Warfare, Information and Cyber, Cranfield UniversityDefence Academy of the United Kingdom, UK*
[2]*Centre for Defence Engineering, Cranfield UniversityDefence Academy of the United Kingdom, UK*
✉Email: alexander.hagelberg@cranfield.ac.uk

Synthetic Aperture Radar (SAR) Coherent Change Detection (CCD) allows for the detection of very small scene changes. This is particularly useful for reconnaissance and surveillance as small changes such as vehicle tracks can be identified. In some situations, it is desirable to rapidly collect repeat pass SAR images for use in change detection, and multistatic geometries may facilitate this. Such repeat passes may however have significant baselines, particularly for satellite-based platforms, though CCD products are reliant on high coherence for good interpretability. This work investigates the sources and levels of incoherence associated with bistatic SAR imagery with increasing baselines using simulations and measured laboratory data.

Introduction: Synthetic Aperture Radar (SAR) allows high-resolution images to be formed. SAR data can also be used interferometrically to determine a Digital Elevation Map (DEM) or to sensitively detect changes within a scene [1]. SAR Coherent Change Detection (CCD) has the potential to detect very small changes such as the tracks made by a vehicle. Typically, the two radar platform trajectories are closely repeated, with a low baseline, for the best possible CCD results [1, 2]. For satellites, this may necessitate long revisit times which may for example lead to decorrelations due to natural processes such as wind and rain [2]. This would reduce CCD interpretability. If planned multistatic SAR satellite constellations [3] come into existence, the ability to utilize trajectories with greater baselines could help reduce revisit times. Such image pairs may potentially have low coherence. This paper investigates the sources and levels of SAR bistatic geometry incoherence through both simulation and laboratory radar measurements.>

Background: SAR image information can be represented in the spatial frequency domain, also known as *K*-space, where it is given the name 'image support' [1]. The extent of the image support is a composite of incident minus scattered wave vectors from transceivers, $\tilde{\mathbf{K}} = \vec{\mathbf{k}}_i - \vec{\mathbf{k}}_s$, to the different scene positions. The length of $\tilde{\mathbf{K}}$ is proportional to frequency, and to the cosine of the bistatic angle [1]. In the context of coherence between SAR images of horizontal terrain the proportion of the overlapping vertically projected image support area to total projected areas (*K*-space overlap) [4] can be used to predict coherence. In the SAR far-field it is straightforward to calculate *K*-space overlap. In the SAR near-field, the *K*-space overlap varies significantly across the scene, complicating the estimation of coherence [1, 5]. The SAR near-field is defined as the regime where the range $d < 2L_{cr}^2/\lambda_c$ for centre wavelength λ_c and for a scene with cross range extent L_{cr}.

SAR coherence between two collections γ_{true} has a value between 0 and 1 and is a little different from the coherence estimated directly from the images $\hat{\gamma}$, which is biased dependent on calculation features such as the CCD estimation window size [4]. γ_{true} can be decomposed into factors which are also in the range 0–1 [1, 2, 4, 6, 7]:

$$\gamma_{true} = \gamma_{temp}\gamma_{SNR}\gamma_{proc}\gamma_{geom} \quad (1)$$

$$\gamma_{proc} = \gamma_{alg}\gamma_{reg} \quad (2)$$

$$\gamma_{geom} = \gamma_{baseline}\gamma_{RCS} \quad (3)$$

In (1) the factors correspond to decorrelations due to: temporal changes between the two collections γ_{temp}; signal-to-noise ratio (SNR) γ_{SNR}; signal processing effects γ_{proc}; and SAR geometry effects γ_{geom}. In (2) the signal processing term γ_{proc} accounts for decorrelations due to the image formation algorithm accuracy γ_{alg} and image registration accuracy γ_{reg}. In (3) the geometry term is decomposed into a calculated baseline correlation term $\gamma_{baseline}$ which accounts for *K*-space overlap; and a Radar Cross Section (RCS) term γ_{RCS}.

Fig. 1 *Image showing the gravel square scene.*

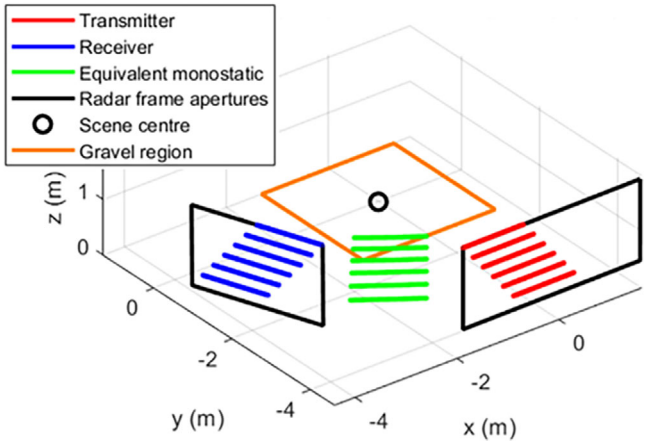

Fig. 2 *Diagram showing measured bistatic SAR geometries and scene dimensions. Each bistatic SAR geometry has transceivers at equal heights and the scene centre is denoted by 'O'. SAR, synthetic aperture radar.*

The RCS term introduced in [8] accounts for a difference in backscattering dependent on imaging geometry, and could incorporate many effects including variation in shadowing, multipath, and polarization. The temporal and baseline correlation terms are typically of most interest for imaged scenes with developed speckle and low baseline [6, 9], however at least for bistatic geometries with high baseline, the RCS term is hypothesized to play a significant role.

Methodology: Bistatic SAR measurements were conducted at the Cranfield University Ground Based SAR laboratory (GBSAR lab) [10]. The scene (Figure 1) consisted of a gravel square 2.7 m × 2.7 m. The measurements were conducted with a Vector Network Analyzer (VNA), with centre frequency of 10 GHz and bandwidth of 4 GHz. Due to the use of a single VNA, there were no signal synchronization issues associated with the bistatic measurements—often a significant issue for practical remote bistatic SAR sensing. The SAR geometries used were constrained by the available transmitter and receiver vertical scanning rectangular apertures pictured in Figure 2 (black), where the scene dimensions and SAR geometries measured are also shown.

For each bistatic SAR geometry, transceiver heights were kept the same and a horizontal aperture of 1.2 m was scanned for both the receiver and transmitter antennas, which gave equivalent monostatic apertures of length 1.12 to 1.18 m. The six bistatic SAR geometry designations used ranged from 'TR1' to 'TR6', with the height progressively decreasing with increasing index (1–6) and bistatic angle progressively increasing—crucially, these geometries were chosen, to maintain a substantial *K*-space overlap between the SAR geometries. It is noted that in previous measurements, variation in grazing angle between bistatic collections did not greatly influence coherence [8].

The transceiver scan geometry parameters are listed in Table 1. It is noted that the grazing and bistatic angles are spatially variant over the scene, and the values provided in the table are calculated to the centre of the scene and gravel region. For TR1 and TR6, there is only a 20-cm overlap (17% of the aperture). The *K*-space overlap between the six SAR geometries was high, with $\gamma_{baseline}$ ranging from 0.83 to 0.98 as seen in Figure 3.

Table 1. Scan geometry parameters for the six bistatic collections.

		TR1	TR2	TR3	TR4	TR5	TR6
Bistatic angle, β (°)		36.5	41.5	46.7	52.1	57.6	63.2
Grazing angle, ψ (°)	Tx	22.1	19.7	17.2	14.6	11.8	8.9
	Rx	22.8	20.4	17.8	15.1	12.2	9.2
	BEM	23.7	21.5	19.2	16.6	13.8	10.7
Range (m)	Tx	5.16	5.02	4.91	4.81	4.73	4.67
	Rx	5.00	4.87	4.75	4.65	4.57	4.51
	BEM	5.08	4.95	4.83	4.73	4.65	4.59
BEM aperture length (m)		1.12	1.14	1.15	1.17	1.18	1.18
Transceiver height (m)		1.94	1.70	1.45	1.21	0.97	0.73
BEM resolution	Range (cm)	4.1	4.0	4.0	4.0	3.9	3.8
	Cross-range (cm)	6.8	6.5	6.3	6.1	6.0	5.9

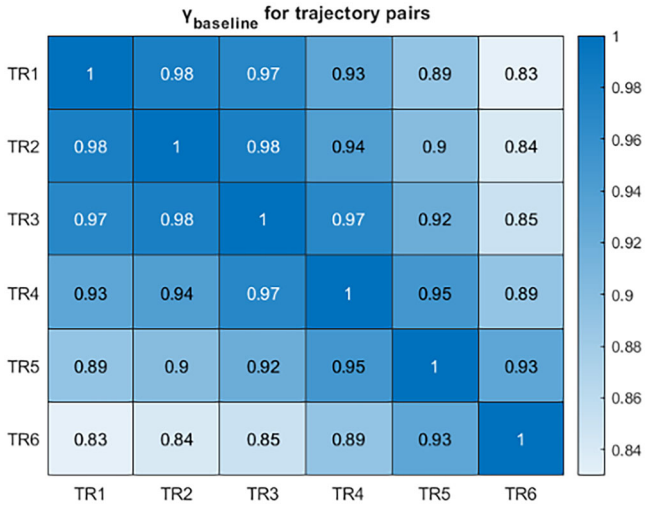

Fig. 3 *Heatmap showing the γ_{baseline} values for the different trajectories.*

Tx denotes the transmitter, Rx the receiver, and BEM the Bistatic Equivalent Monostatic values for the transceiver trajectories. Ranges are in the respective slant planes. Resolutions are in the ground plane and estimated at the scene centre.

In addition to the measurements, simulations were undertaken assuming isotropic point scatterers with a density of approximately 26 scatterers per resolution cell. This provided fully developed SAR speckle. The SAR and CCD processing undertaken was the same for both simulated and measured data.

Results: The coherence of SAR image pairs was calculated as the mean over the CCD image. These mean coherence values were then plotted as a function of the bistatic angle (and by extension grazing angle) difference between the mission and reference trajectories. The measured coherence values are shown in Figure 4. As the separation (baseline) between bistatic trajectories increases, the coherence drops. The coherence also exhibits variation between the polarizations. Additionally, the coherence values of the measured results were then compared against the coherence of the simulated results and with the baseline correlation ($\gamma_{baseline}$). These are also shown in Figure 4. The simulated coherence shows a close match to the $\gamma_{baseline}$; however, the measured results exhibit a coherence which becomes lower with increasing bistatic and grazing angle difference.

Due to the nature of the laboratory environment, Equations (1) to (3) can be simplified to estimate the RCS component: the SNR was high and approximated to 1; no scene changes were present so $\gamma_{temp} = 1$; the measurement ground truth was well known due to the well-controlled antenna positioning and accurate curved wavefront bistatic back-projection

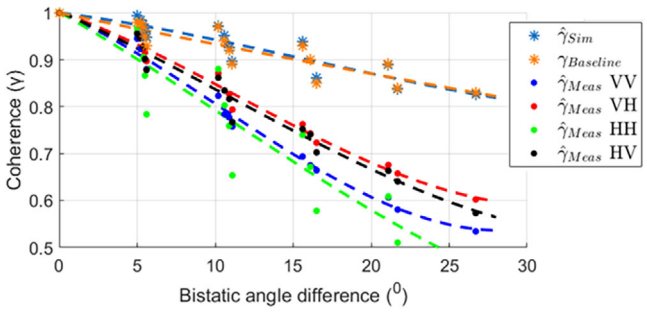

Fig. 4 *Graph of distribution of coherence and $\gamma_{baseline}$ as a function of the difference in the bistatic angle. The measured coherence values for all polarizations are shown in blue. Simulated coherences are shown in red and the baseline correlation in green. A curve of best fit was plotted for each.*

image formation was used, so $\gamma_{algorithm}$ and γ_{reg} are approximated to 1. Hence, the following equation is used to give an *estimate* for γ_{RCS},

$$\hat{\gamma}_{RCS} = \left(\hat{\gamma}_{Meas}(x,y) / \gamma_{baseline}(x,y)\right) \tag{4}$$

The triangular brackets indicate an averaging of the quantities over the scene. It is noted that due to the SAR near-field nature of the measurements, both the $\gamma_{baseline}$ and $\hat{\gamma}_{meas}$ (evaluated within a square sliding window) vary spatially. Hence, they are functions of image coordinates (x, y). Therefore $\hat{\gamma}_{RCS}$ is evaluated as a mean over the spatially varying fraction in (4). '*Meas*' denotes that the coherence value is from the measured data.

An alternative method to estimate $\hat{\gamma}_{\text{RCS}}$ is to use the simulated and measured CCD images directly, that is without the use of $\gamma_{baseline}$. We have

$$\gamma_{Sim} = \gamma_{baseline}\gamma_{alg} \tag{5}$$

$$\gamma_{Meas} = \gamma_{RCS}\gamma_{baseline}\gamma_{alg} \tag{6}$$

where '*Sim*' denotes the simulated values (where $\gamma_{RCS\,Sim}$=1 due to the isotropic scatterer assumption). Hence,

$$\hat{\gamma}_{RCS} = \left(\hat{\gamma}_{Meas}(x,y) / \hat{\gamma}_{Sim}(x,y)\right) \tag{7}$$

As in Equation (4), an averaging over the spatially varying fraction is performed in (7) due to the SAR near-field nature of the measurements. The results for $\hat{\gamma}_{\text{RCS}}$ generated through (7) match those of (4) very closely, owing to the close correspondence of $\hat{\gamma}_{Sim}$ and $\gamma_{baseline}$ as is seen in Figure 5.

In Figure 5, $\hat{\gamma}_{\text{RCS}}$ is plotted for the different geometries and polarizations. $\hat{\gamma}_{\text{RCS}}$ can be seen to drop significantly, with increasing bistatic and elevation angular difference. The decorrelation may be so great that discriminating changes on the ground may not be possible for the greater bistatic angle differences. For bistatic angle differences greater than 10°, coherence is seen to be generally greater in the cross-polarization channels. The HH channel has the least coherence and most variability, which may be due to ground-multipath effects.

The two $\hat{\gamma}_{RCS}$ estimates, (4) and (7), can also be compared with the estimated coherence of spatially variant incoherence trimmed (SVIT) images $\hat{\gamma}_{trimmed}$, which should have a similar value. The *K*-space incoherence-trimming excludes non-*K*-space overlap data from SAR images and is performed for each bistatic collection pair in a computationally intensive spatially variant manner [5, 11].

The comparison of the three approaches is shown in Figure 5 and shows a good agreement. The difference between the results may be due to numerical errors in the calculation of $\gamma_{baseline}$ and in the spatially variant *K*-space trimming process. These are both computationally intensive processes requiring discretization choices.

Conclusion: The results presented show that SAR image speckle regions can suffer significant decorrelation due to differences in bistatic and elevation angles. This is interpreted to be due to the related changes in scattering properties (RCS), even in the presence of high *K*-space overlap. The effect is seen to be an important factor that should be

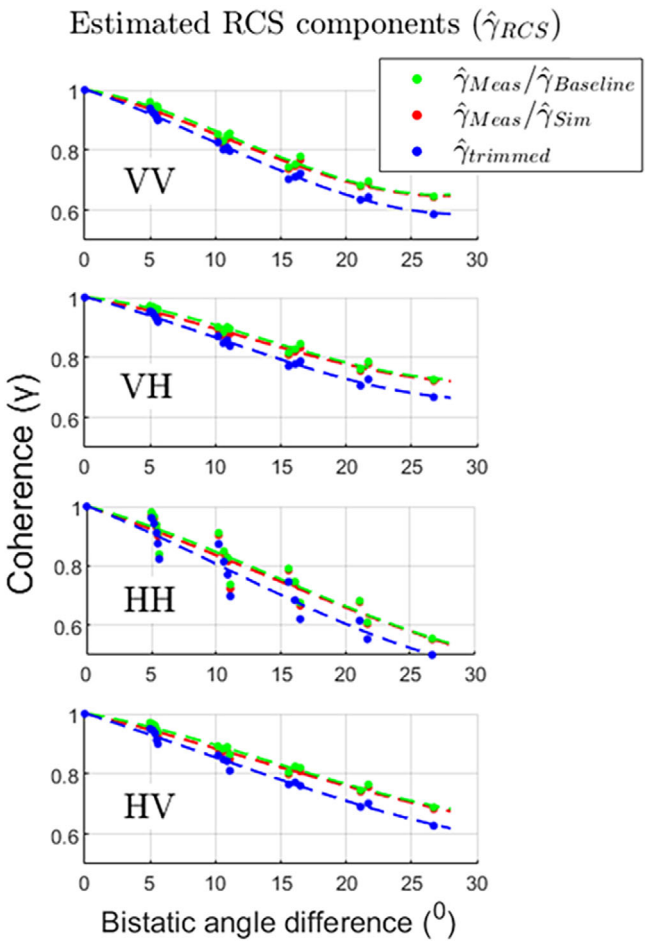

Fig. 5 *Graph showing $\hat{\gamma}_{\mathrm{RCS}}$ estimated with three different methods, plotted against the difference in the bistatic angle. A point was plotted for each pair of radar positions and polarization. A curve of best fit was plotted for each. All four polarizations are shown.*

considered when choosing bistatic SAR CCD geometries. For the bistatic geometries, frequencies, and terrain considered, a difference in bistatic angle of 22° or greater led to a drop in coherence below 0.8, and in some cases below 0.7 (for some in HH polarization). For these bistatic angle differences, there were regions of low coherence which could mistakenly be taken for regions of scene change. When combined with a loss in resolution from the SVIT process, discerning temporal changes with these geometries may become challenging.

Some differences in coherence were seen between the polarimetric channels, such that above a 10° difference in bistatic angle the cross-polarizations showed the highest coherence. This result follows preliminary predictions [12] and it is possible that there may be another polarimetric decomposition that increases coherence further for this type of terrain. Further investigation into the behaviour of the bistatic RCS factor is required, particularly with regard to different ground types and the impact of grazing angle differences, frequency band, and polarimetric decomposition. Corresponding CCD performance analysis experiments [4] would further aid in the interpretation of results.

Credit contribution statement: Alexander Hagelberg: Conceptualization, Formal analysis, Investigation, Methodology, Writing – original draft, Writing – review & editing. Daniel Andre: Conceptualization, Investigation, Methodology, Project administration, Supervision, Writing – review & editing. Mark Finnis: Resources, Software.

Acknowledgements: This paper was produced as a part of research for a PhD sponsored by the Defence Science & Technology Laboratory (DSTL).

Conflict of interest statement: The authors declare no conflict of interest.

Funding information: This work was produced as a part of a PhD funded by the Defence Science & Technology Laboratory (DSTL).

Data availability statement: Radar trajectory co-ordinates will be made available on the Cranfield Online Research Data (CORD) repository. SAR data is the subject of ongoing research but may be made available on request to the corresponding author or the Cranfield GBSAR group

Received: *17 May 2023* Accepted: *31 July 2023*
doi: 10.1049/ell2.12913

References

1 Jakowatz, C.V., Wahl, D.E., Eichel, P.H., Ghiglia, D.C., Thompson, P.A.: *Spotlight-Mode Synthetic Aperture Radar: A Signal Processing Approach*. Kluwer Academic Publishers (1996)
2 Zebker, H.A., Member, S., Villasenor, J.: Decorrelation in interferometric radar echoes. *IEEE Trans. Geosci. Remote Sens.* **30**(5), 950–959 (1992)
3 Airbus: https://www.airbus.com/en/newsroom/press-releases/2019-09-airbus-to-develop-technology-for-ultra-high-resolution-satellites
4 Preiss, M., Stacy, J.: Coherent change detection: Theoretical description and experimental results, defence science and technology organisation (DSTO), Report no. DSTO–TR–1851, (2006)
5 Andre, D., Blacknell, D., Morrison, K.: Spatially variant incoherence trimming for improved SAR CCD. In: SPIE Defense, Security and Sensing, SPIE Defense, Security and Sensing, pp. 153–164 (2013)
6 Wang, Y., Huang, Y., Zha, Y., Pu, W., Yang, J.: Data collection strategies for high quality multi-pass SAR CCD images. In: International Geoscience and Remote Sensing Symposium (IGARSS), Institute of Electrical and Electronics Engineers Inc., pp. 1843–1846 (2014)
7 Bickel, D.L.: SAR Image Effects on Coherence and Coherence Estimation, Sandia National Laboratories, Report no. SAND2014-0369 (2014)
8 Hagelberg, A., Andre, D., Finnis, M.: Polarimetric bistatic SAR image coherence. In: 14th European Conference on Synthetic Aperture Radar, VDE, pp. 80–85 (2022)
9 Doerry, A.W.: Collecting and processing data for high quality CCD images, Sandia National Laboratories, Report no. SAND2007-1545 (2007)
10 Elgy, J., Andre, D., Finnis, M.: Bistatic 3D SAR for wall parameter extraction in cluttered environments. *IET Electron. Lett.* **57**(21), 807–809 (2021)
11 André, D., Blacknell, D., Morrison, K.: Spatially variant incoherence trimming for improved bistatic SAR CCD. In: IEEE Radar Conference, pp. 1–6 (2013)
12 Andre, D.: Bistatic SAR coherence improvement through spatially variant polarimetry. In: IMA Conference on Mathematics in Defence (2015)